Research Square

Preprints are preliminary reports that have not undergone peer review.
They should not be considered conclusive, used to inform clinical practice,
or referenced by the media as validated information.

Reaction-Time-Controlled Ag_2ZnSnS_4 Quantum Dots as Indium-Free Sensitizers for TiO_2 Photoelectrodes

Chang Min Lee
Jeonbuk National University
Woonhyuk Baek
whbaek@jbnu.ac.kr

Jeonbuk National University

Research Article

Keywords: quantum dot-sensitized solar cells (QDSSCs), AZTS, Indium-free, Antisite disorder suppression, Band alignment

Posted Date: November 24th, 2026

DOI: https://doi.org/10.21203/rs.3.rs-11682372/v1

License: This work is licensed under a Creative Commons Attribution 4.0 International License.
Read Full License

Additional Declarations: No competing interests reported.

Abstract

AZTS QDs are proposed as a promising alternative to $CuInSe_2$(CISe) and Cu_2ZnSnS_4(CZTS) QDs. Indium-containing CISe QDs have enabled high-performance quantum dot-sensitized solar cells (QDSSCs), but the limited availability of indium may pose challenges for their large-scale production.[1,2] CZTS QDs, composed of earth-abundant and nontoxic elements, have been explored as an alternative.[3,4] however, Cu-related defects, such as Cu–Zn antisite disorder, can induce charge trapping and band tailing, which limit the performance of CZTS-based QDSSCs.[5,6]

In this study, silver–zinc–tin–sulfide (AZTS) quantum dots (QDs) were synthesized at varying reaction times, and the resulting changes in their optoelectronic properties were investigated. With their environmental compatibility, low toxicity, and potential for defect suppression, AZTS QDs were deposited on mesoporous TiO_2 photoelectrodes for photocurrent measurements, and cross-sectional EDS confirmed their successful loading. Future work will focus on optimizing device conditions, such as core–shell structures and Cu doping, to achieve a sizable photocurrent. This work proposes AZTS QDs as a viable alternative to conventional CISe and CZTS QDs.

1. INTRODUCTION

Quantum dot-sensitized solar cells (QDSSCs) have been extensively investigated owing to their low fabrication costs, size-tunable bandgaps, and high optical absorption coefficients.[7,8] Through impact ionization associated with quantum confinement, quantum dots (QDs) can generate multiple charge carriers upon excitation by a single photon. The theoretical power conversion efficiency of QDSSCs can reach 44%.[9] Indium-based quantum dots, including $CuInSe_2$, have been investigated as sensitizers for QDSSCs, because of their environmentally friendly nature. Zhong and co-workers reported ZCISSe_{2-} quantum dot-sensitized solar cells fabricated using a cation/anion co-alloying strategy, achieving a certified power conversion efficiency of 14.40%.[2] The most widely investigated materials comprise elements that pose sustainability challenges owing to their toxicity or scarcity in the Earth's crust.[10,11] As alternatives to CISe, the quaternary semiconductors Cu_2ZnSnS_4 (CZTS) and $Cu_2ZnSnSe_4$ (CZTSe), which consist of nontoxic and relatively earth-abundant elements, have attracted considerable attention. [3–6,12,13] The optical and electronic properties of ternary and quaternary QDs can be tuned through both particle size and composition. Furthermore, optical bowing may enable these materials to exhibit bandgaps narrower than those of their binary constituents.[14]

Kesterite CZTS (K-CZTS) has been investigated both as an absorber layer in thin-film solar cells and as a sensitizer in QDSSCs owing to its direct bandgap suitable for solar absorption (1.5eV), high absorption coefficient (> $10^4 cm^{-1}$), and excellent photostability.[15–17] A previous study successfully incorporated K-CZTS QDs prepared via a hydrolysis method into QDSSCs. However, the power conversion efficiency of these devices remained limited by their low open-circuit voltage (V_{OC}) and fill factor (FF).[5] Moreover, antisite disorder in K-CZTS can induce charge trapping and suppress photoluminescence (PL), reducing

photocurrent and carrier lifetimes and thereby hindering its use in optoelectronic applications.[6] In CZTS, the similar ionic radii of Cu^+ (78pm) and Zn^{2+} (74pm) promote Cu–Zn antisite disorder, which induces severe electrostatic potential fluctuations and band tailing, manifested as a pronounced red shift in photoluminescence (PL).[18,19] To alleviate this, replacing Cu^+ with the larger Ag^+ (115pm) has been reported to substantially suppress cation site disorder.[20] Consistent with this, the AZTS QDs in this work exhibit PL that was not observed in CZTS nanocrystals, suggesting a reduced probability of exciton trapping at defect sites associated with cation site disorder.[21] This further suggests that the excitons may undergo charge separation and thereby contribute to the photocurrent.

In this work, we report environmentally friendly, low-cost AZTS quantum dot-sensitized solar cells featuring suppressed antisite disorder. To the best of our knowledge, this is the first demonstration of AZTS QD-based solar cells. By tuning the QD size, a key parameter governing their optoelectronic properties, we systematically investigate the size-dependent energy-level alignment between AZTS QDs and mesoporous TiO_2.

2. EXPERIMENTS

2.1. Materials and Reagents

Silver(I) acetate [Ag(OAc)] was purchased from Alfa Aesar. Zinc(II) acetate [$Zn(OAc)_2{\cdot}2H_2O$], tin(IV) chloride [$SnCl_4$, anhydrous], hexamethyldisilathiane [TMS-S], oleylamine (OLA, technical grade 70%), deuterated toluene (tol-d^8,99%), hexane (≥ 99%), toluene (99%) and ethanol (95%) were purchased from Sigma-Aldrich. All chemicals were used as received without further purification.

2.2. Synthetic and Sample Preparation.

The synthesis procedures were adapted with slight modifications from the literature for QDSSCs application.[21] Standard Quadruple-Injection AZTS NC Synthesis. A 15mL 3-neck round-bottom flask was loaded with Ag(OAc) (25mg) and sealed with rubber septa. At the same time, one 20mL scintillation vial was charged with $Zn(OAc)_2{\cdot}2H_2O$(14mg), degassed (2h at 120°C) OLA (1mL) while stirring, and then placed in a sand bath at ∼80°C. Another 20mL scintillation vial was loaded with degassed OLA (1mL) and a stir bar and brought inside a N_2 glovebox to prepare the Sn precursor solution. A micropipet was used to add $SnCl_4$ (9μL) to this vial. It is important to tilt the vial (∼45°) and deliver the $SnCl_4$ onto a dry spot at the bottom of the vial to prevent traces of water in the OLA from hydrolyzing inside of the pipet tip and forming an inconvenient gel. The vial was then quickly capped and taken out of the glovebox. The Sn precursor solution was placed in the same sand bath as the zinc precursor to promote dissolution (∼10min). While the $SnCl_4$ dissolved, two TMS-S solutions were prepared in different 20mL scintillation vials inside the glovebox. The first solution [1] contained toluene (1mL) and TMS-S (13μL), while the second [2] comprised toluene (1mL) and TMS-S (49μL). Each solution was loaded into a labeled 3mL plastic syringe and taken out of the glovebox. This completed the precursor preparation. For the reaction, degassed OLA (3mL) was added to the three- neck round-bottom flask containing the Ag(OAc). This

solution was degassed through three cycles of vacuum-nitrogen at room temperature and rapidly heated to 80°C (12°C/min) under nitrogen and stirring. As the silver solution reaches 65°C, two 1 mL plastic syringes are loaded: one with the tin solution (Sn-OLA) and the other one with the zinc precursor (Zn-OLA), both fully dissolved and pale yellow in color. Once the silver solution reaches 75°C, the heating mantle is removed as well as the existing septum on the flask under a positive nitrogen flow. This septum is quickly replaced by the one holding the four syringes with the precursor solutions. The quadruple injection happens once the reaction reaches 80°C in the order: (1) TMS-S [1], (2) Sn-OLA, (3) TMS-S [2], and (4) Zn-OLA, with ones between injections. In reactions targeting a single size, the flask was cooled (over ∼2min) by blowing cold air at the time chosen to arrest the reaction.

2.3 Characterization and analytical methods

Transmission electron microscopy (TEM). TEM images of the nanomaterials were obtained using an FEI Talos F200X G2 microscope. Energy-dispersive X-ray spectroscopy (EDS) was performed on the same instrument at 10kV.

X-ray diffraction (XRD). XRD patterns were collected on a PANalytical X'Pert PRO powder diffractometer using Cu Kα radiation.

Raman spectroscopy. Raman spectra were collected using a Nanophoton RAMAN Touch microscope. A 532nm diode-pumped solid-state (DPSS) laser with a power of 2mW was used with a 50× objective, and each spectrum was acquired for 10s.

Photoluminescence (PL) and UV–vis–NIR absorption spectroscopy. PL spectra of the solutions/dispersions were measured using a Horiba FluoroMax Plus spectrofluorometer equipped with a Hamamatsu R928P photomultiplier tube detector. UV–vis–NIR absorption spectra of the solutions/dispersions were recorded at room temperature using a Jasco V-770 spectrophotometer installed at the Semiconductor Physics Research Center, Jeonbuk National University.

Ultraviolet Photoelectron Spectroscopy (UPS). UPS measurements were performed using a Thermo Scientific NEXSA G2 photoelectron spectrometer with a helium I (He I) discharge lamp as the excitation source (21.2eV)

Scanning Electron Microscopy - Energy Dispersive X-ray Spectroscopy (SEM–EDS). The cross-sectional morphology and elemental distribution were examined using a field-emission scanning electron microscope (FE-SEM; Carl Zeiss, Gemini500) equipped with an EDS detector. Cross-sectional images were acquired at an accelerating voltage of 15kV. Elemental mapping of Ag(Lα1), Zn(Lα1,2), Sn(Lα1), and S(Kα1) was performed to investigate the spatial distribution of each element across the film layers.

The TEM, EDS, XRD, XPS, Raman, and SEM–EDS measurements were carried out using instruments installed at the Center for University-Wide Research Facilities (CURF) at Jeonbuk National University.

2.4 Electrode assembly

The Cu_2S counter electrode was prepared by immersing brass foil (Alfa Aesar, 0.25mm thick) in HCl solution (DAEJUNG, 35–37 wt%) at 140 ^oC for 30minutes, followed by rinsing with DI water and drying with nitrogen flow. Onto these substrates, an aqueous polysulfide solution of 1M Na_2S and 1M S (99.998%, Aldrich) was dropped to form a porous Cu_2S film on the surface, subsequently rinsed with DI water. The TiO_2/QD working electrode was assembled with the Cu_2S counter electrode using hot melt Surlyn with a thickness of 60mm (Dupont 1702). Then, the aqueous polysulfide electrolyte comprising 1M Na_2S and 1M S was injected into the cells through two small holes pre-drilled at the working electrodes. The active area for each cell was in the range of 0.40 ± 0.03cm^2, which was confirmed using a CCD camera (Moticam 1000) and precisely measured by an image analysis program.

3. RESULTS AND DISCUSSION

In this study, AZTS samples were synthesized with reaction times varied from 30min to 5h to investigate the size-dependent loading behavior of AZTS particles on the photoelectrodes. The synthesis temperature was kept below 80°C to suppress the unintended reduction of Ag. Figure 1 shows a TEM image of the AZTS particles synthesized at 80°C for 30min, which confirms the formation of uniform nanoparticles with a size of approximately 4nm.

Powder X-ray diffraction (XRD) analysis was performed to identify the crystal structure of the synthesized AZTS nanocrystals (Fig. 2). The major diffraction peaks were consistent with the reference pattern of tetragonal AZTS (pirquitasite), a member of the stannite group. With increasing reaction time, the diffraction peaks became sharper and more intense, indicating improved crystallinity. This trend can be interpreted using the Scherrer equation, $D = K\lambda/(\beta \cos\theta)$, where D is the crystallite size, K is the shape factor, λ is the X-ray wavelength, β is the full width at half maximum (FWHM) of the diffraction peak, and θ is the Bragg angle. Because D is inversely proportional to β, the observed decrease in FWHM corresponds to an increase in crystallite size, indicating that the size of the AZTS nanocrystals increased with reaction time. However, some of the AZTS peaks overlap with those of Ag_8SnS_6, which has similar lattice spacings, making it difficult to distinguish the two phases by XRD alone, particularly in nanocrystals where peak broadening is significant. Such ambiguity is not unexpected, as Ag_2S- and Ag_8SnS_6-like phases have been reported as intermediates in the synthesis of AZTS nanocrystals.

Thus, while XRD was used to confirm the crystal structure and the size evolution of the AZTS nanocrystals, Raman spectroscopy was additionally performed to examine the possible presence of an Ag_8SnS_6 secondary phase (Fig. 3). AZTS nanocrystals have been reported to show characteristic Raman peaks at 345 and 365cm^{-1}, and the spectra of our samples exhibited features in this region, consistent with the formation of AZTS. In contrast, no distinct peak was observed near 309cm^{-1}, the strongest known mode of bulk canfieldite (Ag_8SnS_6), which appears prominently when the Zn precursor is omitted from the synthesis. Accordingly, no Raman evidence of an Ag_8SnS_6 secondary phase was detected under the present measurement conditions. Taken together with the XRD results, these findings support the formation of the target AZTS QDs.

The PL peak of the AZTS QDs shifted toward longer wavelengths as the reaction time increased (Fig. 4a), indicating that the emission can be tuned by controlling the particle size. The absorption edge showed the same trend, shifting from 709nm to 793nm with increasing reaction time (Fig. 4b). The band gaps, estimated from Tauc plots derived from the absorption spectra (Fig. 4b), corresponded to 709nm(1.75eV), 722nm(1.72eV), 752nm(1.65eV), and 793nm(1.56eV) for the QDs synthesized for 30min, 1h, 2h, and 5h, respectively, showing a monotonic decrease with reaction time. Because the band gap of QDs depends on their size, larger QDs emit and absorb at longer wavelengths and thus harvest a broader portion of the solar spectrum. Overall, the band gaps decreased from approximately 1.75eV to 1.56eV, covering the red to near-infrared boundary region.

This range is advantageous for photovoltaic applications. Since the optimum band gap of a single-junction solar cell is approximately 1.34eV(≈ 925nm), absorption extending from the visible toward the near-infrared (NIR) region allows more photons to be absorbed while keeping the voltage loss moderate. In particular, about half of the solar spectrum lies in the infrared region, which cannot be utilized by sensitizers absorbing only visible light. In addition, band gaps of 1.7–1.8eV are considered optimal for the wide-band-gap top cell in tandem devices, and the tunable edge of the AZTS QDs allows access to this range. This tunability therefore suggests that AZTS QDs can be exploited in designs aimed at extending the solar absorption range.

However, a tunable band gap alone does not guarantee a small voltage loss, because the quality of the band edges is equally important. In CZTS, high densities of charged defects cause band tailing, in which electrostatic potential fluctuations create localized tail states below the conduction band minimum and above the valence band maximum. The tail states introduced by these fluctuations reduce the effective band gap of the absorber, which in turn lowers the open-circuit voltage (V_{oc}) of the solar cell. Band tailing is therefore regarded as a major contributor to the large V_{oc} deficit that limits CZTS-based devices. Because carriers relax into these tail states before recombining, band tailing is manifested as a red shift of the photoluminescence (PL) peak to lower energy relative to the band gap (E_g) in CZTS, this red shift is pronounced (190meV). The deep defect levels of the acceptor Cu_{Zn} and the donor Zn_{Cu}, the resulting large potential fluctuations in the band structure, and the high density of interface defects are suggested to limit the efficiency of CZTS solar cells. [18,19]

In contrast, the PL peak of the AZTS QDs lies close to the absorption edge in all samples (Fig. 4.a), and the small energy difference between them indicates that carrier relaxation into tail states is limited. This behavior suggests that band tailing is suppressed in the AZTS QDs, which is favorable for reducing voltage loss and charge trapping when the QDs are used as sensitizers.

To investigate the energy-level alignment between the AZTS QDs and TiO_2, ultraviolet photoelectron spectroscopy (UPS) was performed (Fig. 5a). The work function, determined from the secondary-electron cut-off, and the valence band onset were 4.37 and 0.43eV for the 30min sample, 4.58 and 0.44eV for 1h, 4.63 and 0.49eV for 2h, and 4.78 and 0.33eV for 5h, respectively. From these values, the valence band maximum (VBM) was located at − 4.80, − 5.02, − 5.12, and − 5.11eV for the 30min, 1h, 2h,

and 5h samples, respectively. The conduction band minimum (CBM) was then obtained by adding the optical band gaps determined from the Tauc plots to the VBM, yielding − 3.05, − 3.30, − 3.47, and − 3.55eV, respectively (Table 1).

Table 1
Work function (Φ), valence band onset, valence band maximum (VBM), optical band gap (E_g), and conduction band minimum (CBM) of the AZTS QDs synthesized for different reaction times. The VBM was calculated as − (Φ + onset), and the CBM was obtained by adding E_g determined from the Tauc plots to the VBM.

Reaction time	Φ(eV)	Onset(eV)	VBM(eV)	E_g(eV)	CBM(eV)
30min	4.37	0.43	-4.80	1.75	-3.05
1h	4.58	0.44	-5.02	1.72	-3.30
2h	4.63	0.49	-5.12	1.65	-3.47
5h	4.78	0.33	-5.11	1.56	-3.55

The relative band positions of TiO_2 and the AZTS QDs are illustrated in Fig. 5b. TiO_2 has a CBM of − 4.05eV, a VBM of − 7.20eV, and a band gap of about 3.2eV. As the particle size decreased, both band edges of the AZTS QDs shifted toward the vacuum level (upward), consistent with quantum confinement. The upward shift of the CBM (0.50eV from 5h to 30min) was larger than that of the VBM (0.31eV), which is in line with the lighter effective mass of electrons than that of holes. In all samples, the CBM of the AZTS QDs lies above that of TiO_2, with CBM offsets of 1.00, 0.75, 0.58, and 0.50eV for the 30min, 1h, 2h, and 5h samples, respectively. This indicates that the band alignment is favorable for electron injection from the AZTS QDs into TiO_2 and that the driving force for injection increases as the particle size decreases.

To increase the amount of AZTS QDs loaded onto the TiO_2 electrodes, the QDs were synthesized at a five-fold higher precursor concentration (×5) and then loaded onto the TiO_2 electrodes. Figure 6a shows photographs of the bare TiO_2 film and the films loaded with AZTS QDs synthesized at different reaction times, arranged in the order of increasing reaction time. QDs synthesized at reaction times of 30min, 1h, 2h, and 5h were used for comparison, and the corresponding electrodes are denoted as AZTS-30min/TiO_2, AZTS-1h/TiO_2, AZTS-2h/TiO_2, and AZTS-5h/TiO_2, respectively. Following the loading, scanning electron microscopy–energy-dispersive X-ray spectroscopy (SEM–EDS) analysis was performed to examine the surface morphology of the electrodes and the spatial distribution of the AZTS constituent elements (Fig. 6.b–e for AZTS-30min/TiO_2, AZTS-1h/TiO_2, AZTS-2h/TiO_2, and AZTS-5h/TiO_2, respectively). EDS analysis detected Ti and O signals from the TiO_2 electrodes, together with Ag, Zn, Sn, and S signals from AZTS, in all samples. Furthermore, EDS elemental mapping showed that the Ag, Zn, Sn, and S signals spatially coincided with the TiO_2 regions of the electrodes, indicating a distribution of the AZTS constituent elements throughout the TiO_2 electrodes. These results confirm that AZTS QDs synthesized at each reaction time were successfully loaded onto the TiO_2 electrodes.

4. CONCLUSION

In this study, AZTS quantum dots (QDs) of different sizes were synthesized by varying the reaction time from 30min to 5h, and the increase in particle size with reaction time was confirmed by XRD. The XRD and Raman results were consistent with the tetragonal AZTS crystal structure, and no Raman evidence of an Ag_8SnS_6 secondary phase was detected. The absorption edge of the AZTS QDs shifted from 709nm to 793nm with increasing reaction time, and a comparison of the PL peaks with the band gaps obtained from Tauc plots showed that the PL peak lies close to the absorption edge, indicating that band tailing, which is commonly observed in CZTS, is suppressed in the AZTS QDs. The energy-level alignment between the AZTS QDs and TiO_2, determined by UPS, showed that the CBM of the AZTS QDs lies above that of TiO_2 in all samples, thereby confirming that efficient electron injection from the AZTS QDs into TiO_2 is energetically favorable. Furthermore, the AZTS QDs were successfully loaded onto mesoporous TiO_2 electrodes, and SEM–EDS analysis revealed the distribution of the AZTS constituent elements on the electrodes, supporting the incorporation of each sample. Future work will focus on optimizing device conditions, such as introducing core–shell structures and Cu doping, to further enhance the potential of AZTS QDs as sensitizers. Overall, this work proposes AZTS QDs as a promising alternative to conventional CISe and CZTS QDs.

Declarations

Author Contribution

C.L and W.B wrote the manuscript and reviewed the manuscript.

Acknowledgement

C. M. and W. B. was supported by research funds for newly appointed professors of Jeonbuk National University in 2024, Korea Basic Science Institute (National research Facilities and Equipment Center) grant funded by the Ministry of Education (grant No. RS-2024-00436672), and Global - Learning & Academic research institution for Master's·PhD students, and Postdocs (LAMP) Program of the National Research Foundation of Korea (NRF) grant funded by the Ministry of Education (No. RS-2024-00443714).

References

1. Li, W. P., Zhenxiao; Zhong, Xinhua, $CuInSe_2$ and $CuInSe_2$–ZnS based high efficiency "green" quantum dot sensitized solar cells. Journal of Materials Chemistry A,**3**,1649–1655(2015).
2. Song, H. L., Yu; Zhou, Mengsi; Rao, Huashang; Pan, Zhenxiao; Zhong, Xinhua, Zn-Cu-In-S-Se Quinary "Green" Alloyed Quantum-Dot-Sensitized Solar Cells with a Certified Efficiency of 14.4%. Angewandte Chemie International Edition,**60**,6137–6144(2021).

3. Xu, J. Y., Xia; Yang, Qing-Dan; Wong, Tai-Lun; Lee, Chun-Sing, Cu_2ZnSnS_4 Hierarchical Microspheres as an Effective Counter Electrode Material for Quantum Dot Sensitized Solar Cells. The Journal of Physical Chemistry C,**116**,19718–19723(2012).
4. Steinhagen, C. P., Matthew G.; Akhavan, Vahid; Goodfellow, Brian; Koo, Bonil; Korgel, Brian A., Synthesis of Cu_2ZnSnS_4 Nanocrystals for Use in Low-Cost Photovoltaics. Journal of the American Chemical Society,**131**,12554–12555(2009).
5. Bai, B. K., Dongxing; Zhou, Wenhui; Zhou, Zhengji; Wu, Sixin, Application of quaternary Cu_2ZnSnS_4 quantum dot-sensitized solar cells based on the hydrolysis approach. Green Chemistry,**17**,4377–4382(2015).
6. Kattan, N. A. G., I. J.; Cherns, D.; Fermin, D. J., Observation of antisite domain boundaries in Cu_2ZnSnS_4 by atomic-resolution transmission electron microscopy. Nanoscale,**8**,14369–14373(2016).
7. Kim, J.-Y. Y., Jiwoong; Yu, Jung Ho; Baek, Woonhyuk; Lee, Chul-Ho; Son, Hae Jung; Hyeon, Taeghwan; Ko, Min Jae, Highly Efficient Copper–Indium–Selenide Quantum Dot Solar Cells: Suppression of Carrier Recombination by Controlled ZnS Overlayers. ACS Nano,**9**,11286–11295(2015).
8. Yang, J. K., Jae-Yup; Yu, Jung Ho; Ahn, Tae-Young; Lee, Hyunjae; Choi, Tae-Seok; Kim, Young-Woon; Joo, Jin; Ko, Min Jae; Hyeon, Taeghwan, Copper–indium–selenide quantum dot-sensitized solar cells. Physical Chemistry Chemical Physics,**15**,20517–20525(2013).
9. Hanna, M. C. N., A. J., Solar conversion efficiency of photovoltaic and photoelectrolysis cells with carrier multiplication absorbers. Journal of Applied Physics,**100**,074510(2006).
10. Grim, J. Q. M., Liberato; Moreels, Iwan, A sustainable future for photonic colloidal nanocrystals. Chemical Society Reviews,**44**,5897–5914(2015).
11. Chopra, S. S. T., Thomas L., Comparative cradle-to-gate energy assessment of indium phosphide and cadmium selenide quantum dot displays. Environmental Science: Nano,**4**,244–254(2017).
12. Kişnişci, Z. Ö., Faruk; Tuğluoğlu, Nihat; Yüksel, Ömer Faruk, Structural and optical properties of $Cu_2ZnSnSe_4$ nanocrystals thin film. Optical and Quantum Electronics,**56**,1239(2024).
13. Singh, N. M., Vignesh; Nemala, Sivasankar; Mallick, Sudhanshu; Angaiah, Subramania, $Cu_2ZnSnSe_4$ QDs sensitized electrospun porous TiO_2 nanofibers as photoanode for high performance QDSC. Solar Energy,**171**,571–579(2018).
14. Pan, Z. Z., Ke; Wang, Jin; Zhang, Hua; Feng, Yaoyu; Zhong, Xinhua, Near Infrared Absorption of $CdSe_xTe_{1-x}$ Alloyed Quantum Dot Sensitized Solar Cells with More than 6% Efficiency and High Stability. ACS Nano,**7**,5215–5222(2013).
15. Riha, S. C. P., Bruce A.; Prieto, Amy L., Solution-Based Synthesis and Characterization of Cu_2ZnSnS_4 Nanocrystals. Journal of the American Chemical Society,**131**,12054–12055(2009).
16. Jimbo, K. K., Ryoichi; Kamimura, Tsuyoshi; Yamada, Satoru; Maw, Win Shwe; Araki, Hideaki; Oishi, Koichiro; Katagiri, Hironori, Cu_2ZnSnS_4-type thin film solar cells using abundant materials. Thin Solid Films,**515**,5997–5999(2007).

17. Katagiri, H., Cu_2ZnSnS_4 thin film solar cells. Thin Solid Films,**480-481**,426–432(2005).
18. Gokmen, T. G., Oki; Todorov, Teodor K.; Mitzi, David B., Band tailing and efficiency limitation in kesterite solar cells. Applied Physics Letters,**103**,103506(2013).
19. Yin, L. C., Guanming; Feng, Ye; Li, Zhaohui; Yang, Chunlei; Xiao, Xudong, Limitation factors for the performance of kesterite Cu_2ZnSnS_4 thin film solar cells studied by defect characterization. RSC Advances,**5**,40369–40374(2015).
20. Saha, A., Figueroba, A. & Konstantatos, G., Ag_2ZnSnS_4 Nanocrystals Expand the Availability of RoHS Compliant Colloidal Quantum Dots. Chemistry of Materials,**32**,2148–2155(2020).
21. Villanueva, F. Y. H., Minhal; Green, Philippe B.; Imperiale, Christian J.; Rahman, Samihat; Burns, Darcy C.; Wilson, Mark W. B., A Stepwise Reaction Achieves Ultrasmall Ag_2ZnSnS_4 Nanocrystals. ACS Nano,**18**,35182–35201(2024).

Figures

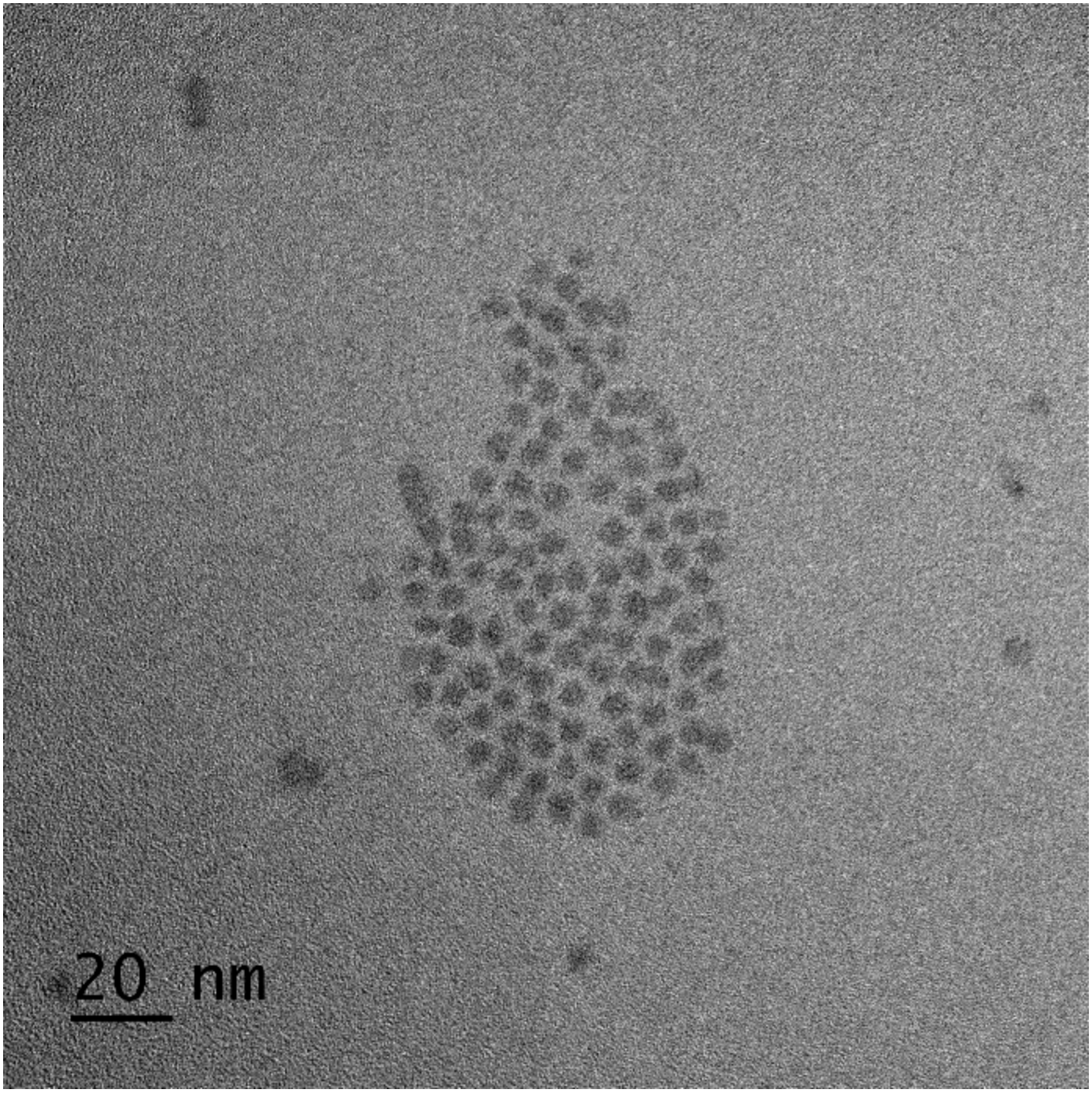


Figure 1

TEM image of the AZTS QDs synthesized at a reaction time of 5 h. The QDs are well dispersed and have an average size of approximately 4 nm.

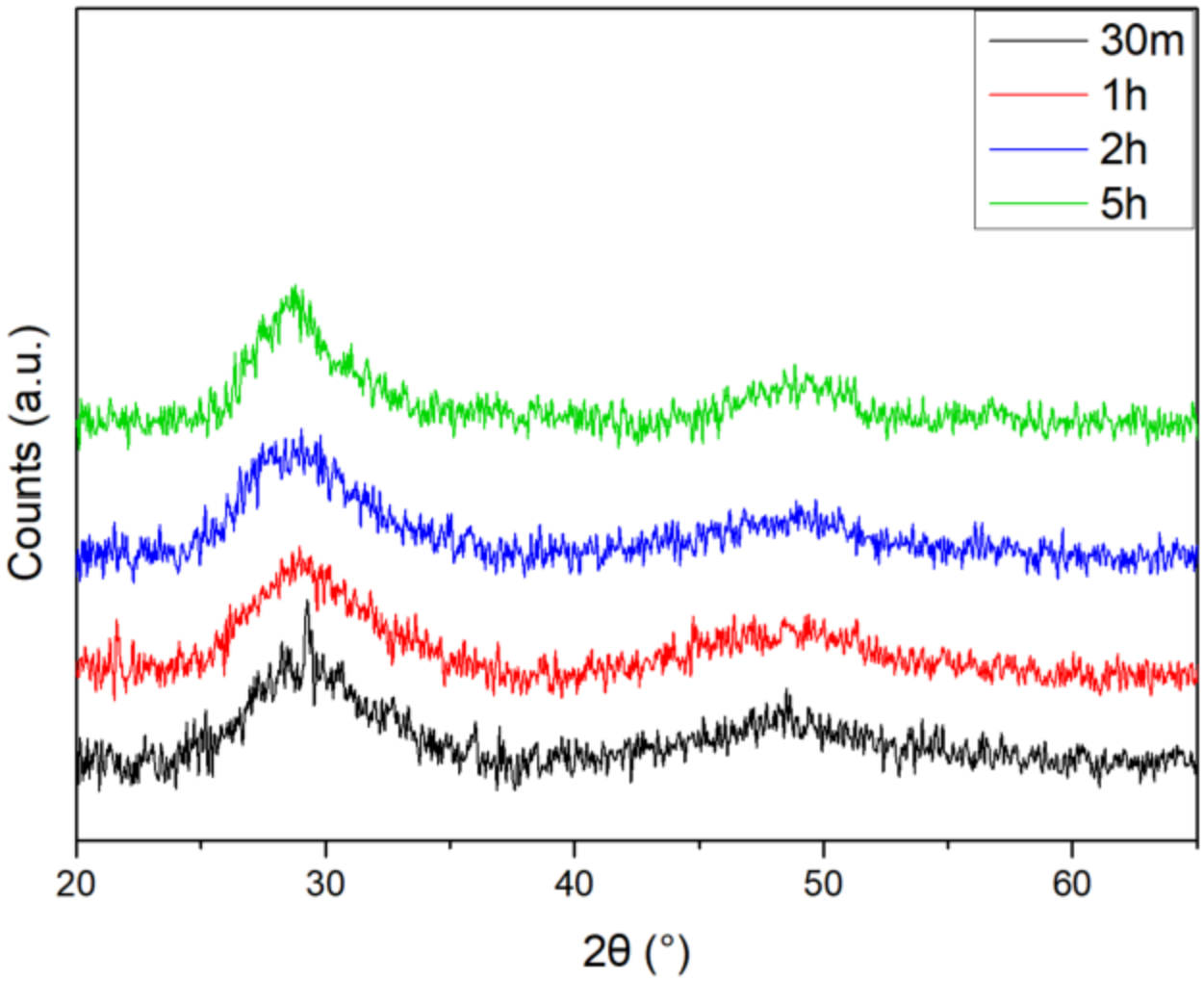


Figure 2

XRD patterns of AZTS QDs synthesized at different reaction times (30min, 1h, 2h, and 5h).

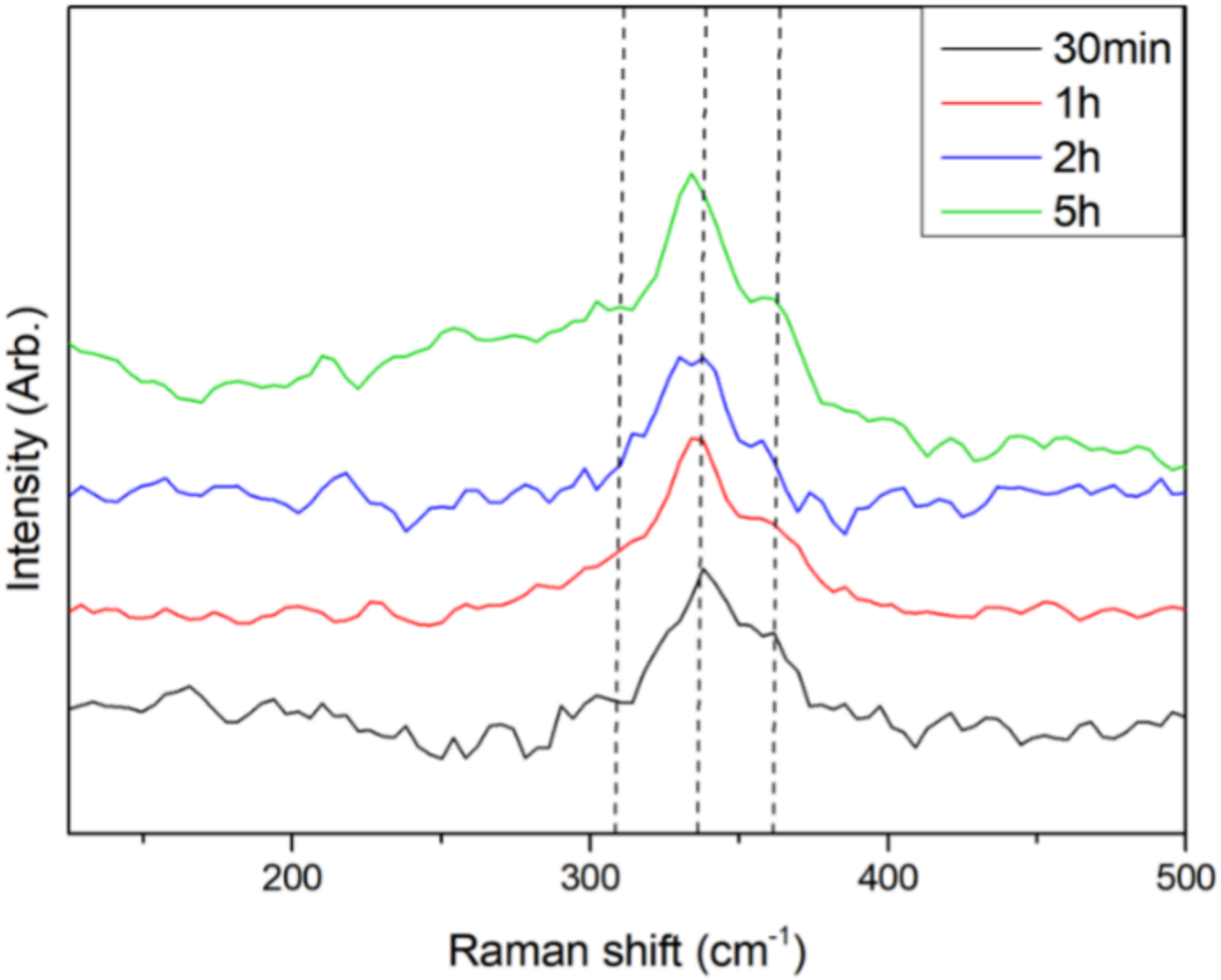


Figure 3

Raman spectra of AZTS QDs synthesized at reaction times of 30min, 1h, 2h, and 5h. The dashed lines indicate the characteristic Raman peaks of AZTS at 345 and 365cm^{-1} and the strongest mode of bulk canfieldite Ag_8SnS_6 at 309cm^{-1}.

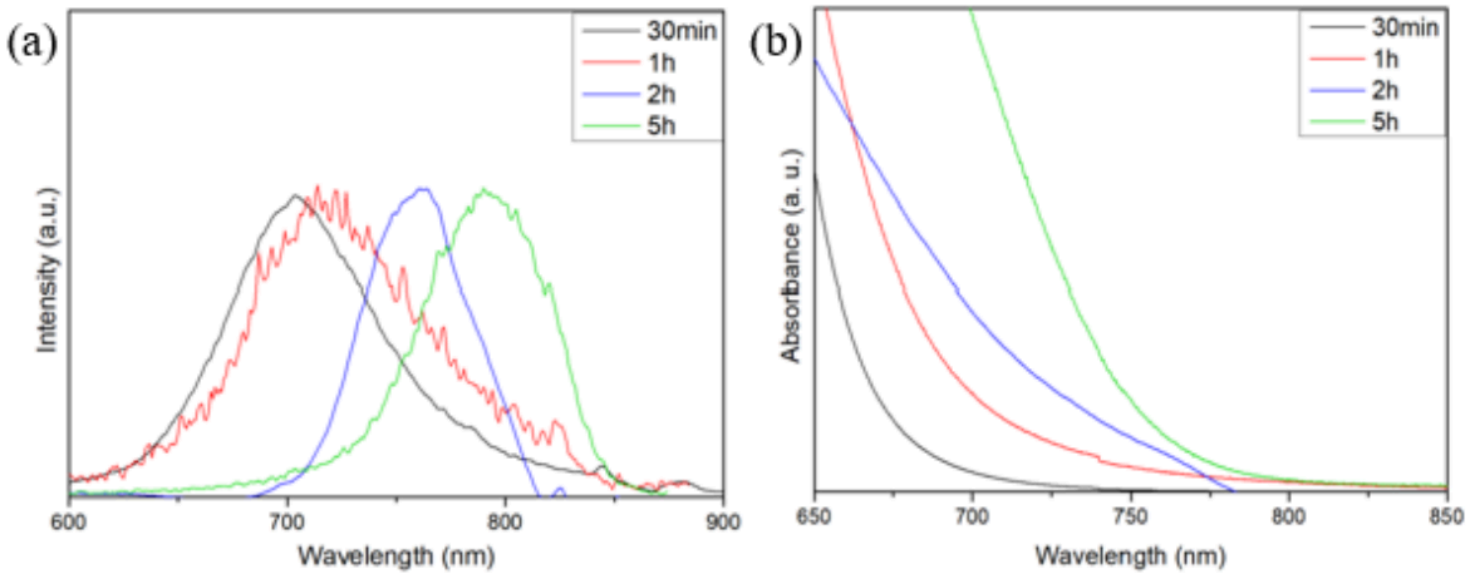


Figure 4

(a) Normalized photoluminescence (PL) spectra and **(b)** absorption spectra of AZTS QDs synthesized at reaction times of 30min, 1h, 2h, and 5h. With increasing reaction time, both the PL peak and the absorption edge shift toward longer wavelengths.

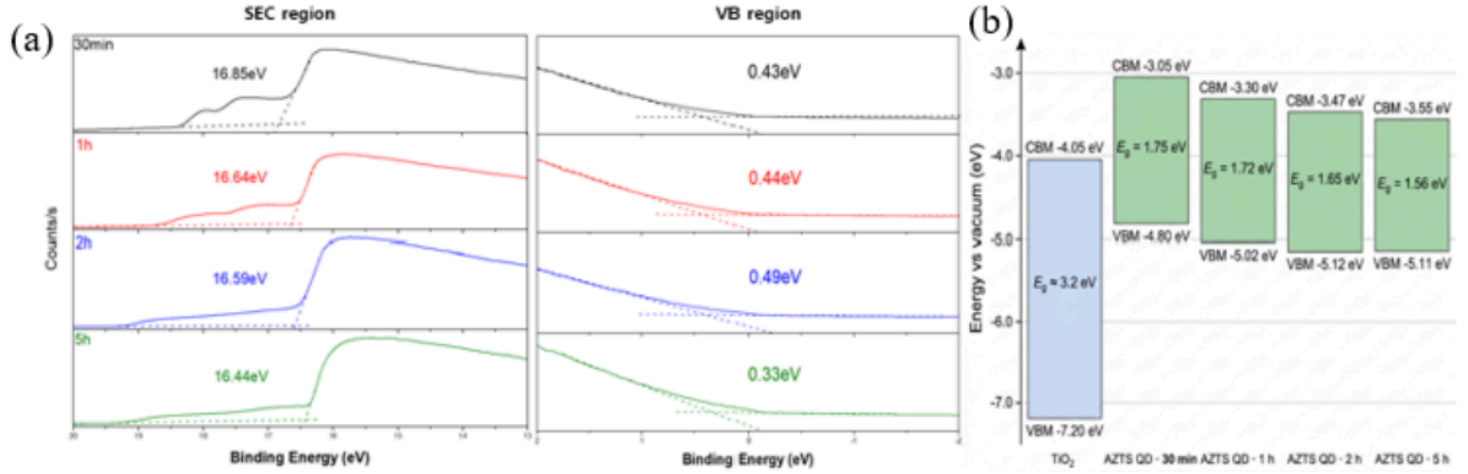


Figure 5

(a) UPS spectra of the AZTS QDs synthesized for 30min, 1h, 2h, and 5h: secondary-electron cut-off (SEC) region and valence band (VB) onset region measured with He I (21.22eV) radiation. The dashed lines indicate the linear extrapolations used to determine the cut-off and onset energies. **(b)** Energy-level diagram of TiO_2 and the AZTS QDs with respect to the vacuum level.

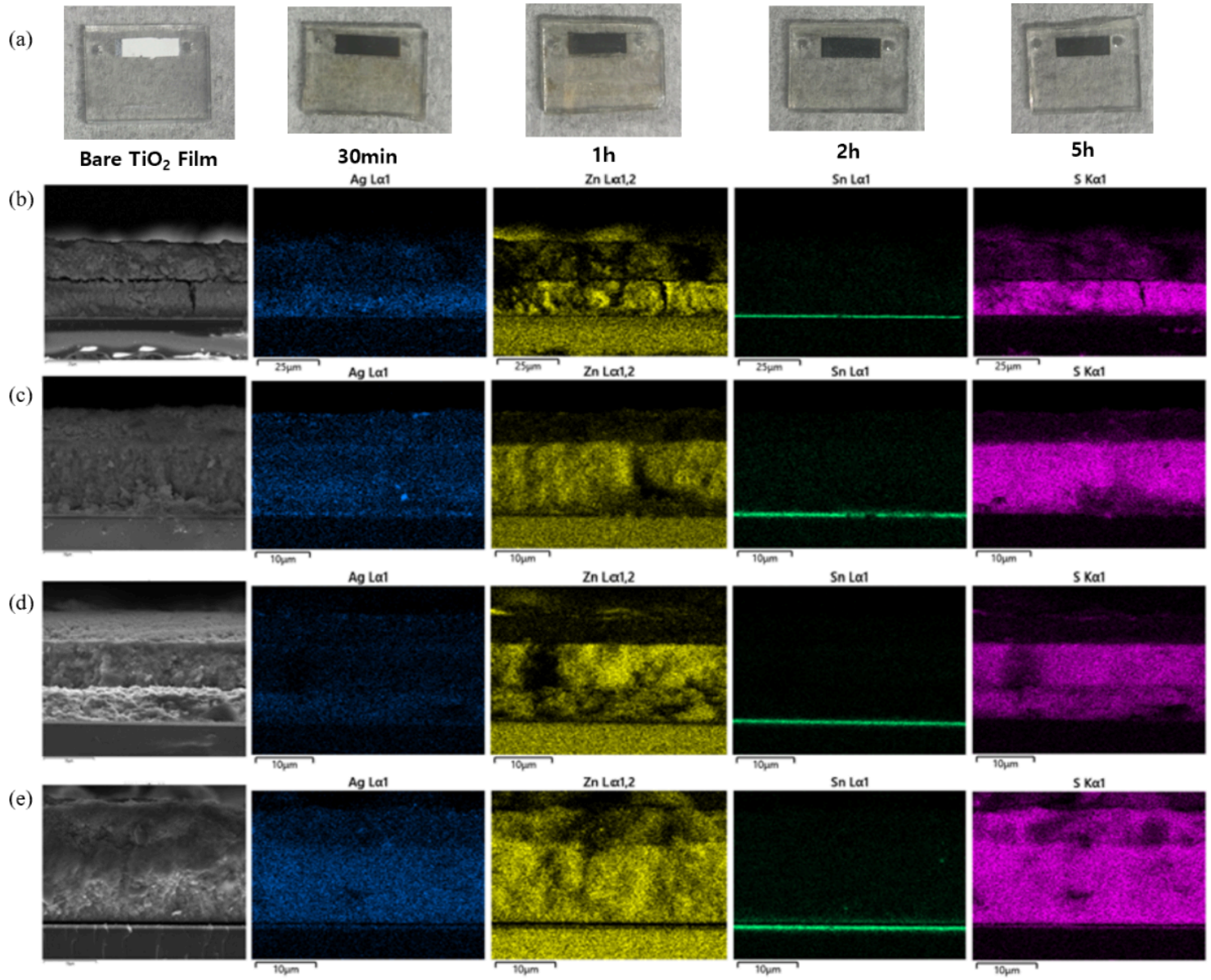


Figure 6

(a) Photographs of the bare TiO_2 film and the AZTS-sensitized TiO_2 films loaded with AZTS QDs synthesized at different reaction times, arranged in the order of increasing reaction time. SEM–EDS analysis of **(b)** AZTS-30min/TiO_2, **(c)**AZTS-1h/TiO_2, **(d)** AZTS-2h/TiO_2, and **(e)** AZTS-5h/TiO_2.